AGU PUBLICATIONS

JGR

Journal of Geophysical Research: Space Physics

RESEARCH ARTICLE
10.1002/2015JA021572

Key Points:
- Pi2 travel with DFs until the DFs slow in the braking region and the Pi2 begin to run ahead of them
- Ionospheric parameters strongly affect how Pi2 are able to propagate
- Both the UCLA and LFM models show similar results for Pi2 propagation outside of ~−7 *RE*

Supporting Information:
- Movie S1
- Caption for Movie S1

Correspondence to:
J. B. Ream,
jodiebt@ucla.edu

Citation:
Ream, J. B., R. J. Walker, M. Ashour-Abdalla, M. El-Alaoui, M. Wiltberger, M. G. Kivelson, and M. L. Goldstein (2015), Propagation of Pi2 pulsations through the braking region in global MHD simulations, *J. Geophys. Res. Space Physics*, *120*, 10,574–10,591, doi:10.1002/2015JA021572.

Received 15 JUN 2015
Accepted 8 DEC 2015
Accepted article online 13 DEC 2015
Published online 29 DEC 2015

Propagation of Pi2 pulsations through the braking region in global MHD simulations

J. B. Ream[1], R. J. Walker[1], M. Ashour-Abdalla[2], M. El-Alaoui[2], M. Wiltberger[3], M. G. Kivelson[1,4], and M. L. Goldstein[5]

[1]Department of Earth, Planetary and Space Sciences, University of California, Los Angeles, California, USA, [2]Department of Physics and Astronomy, University of California, Los Angeles, California, USA, [3]High Altitude Observatory, National Center for Atmospheric Research, Boulder, Colorado, USA, [4]Department of Atmospheric, Oceanic and Space Sciences, University of Michigan, Ann Arbor, Michigan, USA, [5]Heliospheric Physics Laboratory, Goddard Space Flight Center, Greenbelt, Maryland, USA

Abstract We investigate the propagation of Pi2 period pulsations from their origin in the plasma sheet through the braking region, the region where the fast flows are slowed as they approach the inner edge of the plasma sheet. Our approach is to use both the University of California, Los Angeles (UCLA) and Lyon-Fedder-Mobarry (LFM) global magnetohydrodynamic (MHD) computer codes to simulate the Earth's magnetosphere during a substorm that occurred on 14 September 2004 when Pi2 pulsations were observed. We use two different MHD models in order to test the robustness of our conclusions about Pi2. The simulations are then compared with ground-based and satellite data. We find that the propagation of the pulsations in the simulations, especially through the braking region, depends strongly on the ionospheric models used at the inner boundary of the MHD models. With respect to typical observed values, the modeled conductances are high in the UCLA model and low in the LFM model. The different conductances affect the flows, producing stronger line tying that slows the flow in the braking region more in the UCLA model than in the LFM model. Therefore, perturbations are able to propagate much more freely into the inner magnetosphere in the LFM results. However, in both models Pi2 period perturbations travel with the dipolarization front (DF) that forms at the earthward edge of the flow channel, but as the DF slows in the braking region, $-8 \leq x \leq -6\ R_E$, the Pi2 period perturbations begin to travel ahead of it into the inner magnetosphere. This indicates that the flow channels generate compressional waves with periods that fall within the Pi2 range and that, as the flows themselves are stopped in the braking region, the compressional wave continues to propagate into the inner magnetosphere.

1. Introduction

ULF waves observed on the ground at substorm onset with periods between 40 and 150 s, categorized as Pi2 pulsations, have been observed and studied for over 50 years. Because the pulsations are observed concurrently with substorm onset, they are often used to determine the precise onset time and location of substorms, [e.g., *Saito et al.*, 1976; *Sakurai and Saito*, 1976; *Olson*, 1999; *Miyashita et al.*, 2000; *Kepko et al.*, 2004; *Hsu and McPherron*, 2007; *Kim et al.*, 2007; *Keiling et al.*, 2008]; however, there is currently no consensus on how and where the pulsations themselves are generated in the magnetosphere. A recent review of Pi2 by *Keiling and Takahashi* [2011] lists seven different models for Pi2 generation. The source regions described in these models range from the reconnection region in the tail to the plasmasphere, and each describes a different mechanism for generating the pulsations.

In the tail models the Pi2 frequencies are inherent to the flow channel (bursty flow model [*Kepko et al.*, 2001], described below) or the reconnection region itself (pulsed reconnection model [*Keiling et al.*, 2006]), or they are generated by plasma instabilities in the near-Earth plasma sheet (instability-driven model [*Solovyev et al.*, 2000; *Keiling et al.*, 2008]). In the bursty flow model [*Kepko and Kivelson*, 1999; *Kepko et al.*, 2001, 2004], bursty bulk flows (BBFs), which are plasma flows in the tail with $v_x > 100$ km/s [*Angelopoulos et al.*, 1992, 1994] produced by reconnection in the near-Earth plasma sheet, generate Pi2 period pulsations as they travel earthward. The bursty flow model separates Pi2 into three distinct categories: transient response (TR), inertial current (IC), and directly driven (DD). As BBFs propagate earthward from the reconnection region they send Alfvén waves along the field lines into the ionosphere. Due to an impedance mismatch between the plasma

sheet and the ionosphere, part of that signal is reflected. This generates a bouncing Alfvén wave on the field lines associated with the fast flow. From the ground, this bouncing Alfvén wave would be observed as Pi2 pulsations at high latitudes since it is linked to the relatively distant tail. This source for Pi2 pulsations was first discussed by *Southwood and Stuart* [1980], and it is included in the bursty flow model as the source for TR Pi2.

As BBFs propagate into the braking region and approach the inner edge of the plasma sheet, the dipolarization front signature in B_z diminishes as the flow speed decreases to background levels. IC Pi2 are generated by time variations in the flow velocity in the braking region [*Shiokawa et al.*, 1997; *Yumoto et al.*, 1989; *Nagai et al.*, 1998; *Kepko et al.*, 2001]. Both TR and IC Pi2 pulsations are associated with the substorm current wedge *McPherron* [1972]. However, they have slightly different signatures on the ground. Specifically, TR Pi2 have a damped sinusoidal form that continues after the driving flow has stopped, and IC Pi2 have a relatively constant amplitude and are only present while the flows are present. In addition, the waveforms of the IC Pi2 match the flow variations in the magnetotail while the TR Pi2 waveforms do not [*Kepko and Kivelson*, 1999; *Kepko et al.*, 2001].

For the disturbance generated by the flow channels to be observable on the ground at middle to low latitudes, the disturbance must continue propagating earthward from the inner edge of the plasma sheet to low L shells. In the bursty flow model, when the BBFs reach the inner edge of the plasma sheet, they generate a compressional pulse that continues to travel earthward into the inner magnetosphere. Trains of flow bursts generate packets of compressional pulses that travel earthward, coupling to the shear wave at low L shells and are observed on the ground at middle to low latitudes. These perturbations make up the DD category of Pi2 pulsations.

Another model for the generation of Pi2 pulsations in the magnetotail is the instability-driven model [*Solovyev et al.*, 2000; *Keiling et al.*, 2008; *Keiling*, 2012]. *Keiling* [2012] specifically identifies the drifting ballooning mode in the near-Earth plasma sheet as the source for Pi2 period pulsations measured on the ground. Pulsations generated through this mechanism would be observed at high latitudes and could potentially coexist with Pi2 generated through the transient response mechanism described above.

The set of models that describe Pi2 generation by mechanisms in the magnetotail account mainly for Pi2 pulsations observed at high latitudes on the ground. The bursty flow model also includes a mechanism for the generation of middle- to low-latitude Pi2 pulsations via the directly driven (DD) category of Pi2. There are several additional models that can account for middle- to low-latitude Pi2 pulsations. Each of the models for Pi2 generation in the inner magnetosphere requires that a disturbance in the tail must impact the inner edge of the plasma sheet, exciting a compressional wave that travels earthward. The Pi2 frequencies are then selected out by some mechanism in the inner magnetosphere. Some of the candidates for Pi2 selection in the inner magnetosphere are plasmasphere cavity modes [*Saito and Matsushita*, 1968; *Yeoman and Orr*, 1989; *Sutcliffe and Yumoto*, 1991; *Takahashi et al.*, 1992], plasmasphere virtual resonance (PVR) [*Fujita et al.*, 2002], and plasmapause surface waves [*Chen and Hasegawa*, 1974; *Sutcliffe*, 1975; *Southwood and Stuart*, 1980]. The difference between these models and the bursty flow model is the source of the Pi2 period in the magnetic pulsations. The bursty flow model attributes the period of the pulsations directly to the flow bursts, while the inner magnetosphere models attribute the period to wave modes associated with the plasmasphere. Observations of Pi2 by *Uozumi et al.* [2009] verify the existence of shear waves that are generated by a compressional wave in agreement with the directly driven model for generation of middle- to low-latitude Pi2.

Each of the existing Pi2 models is based on satellite and ground-based observations. However, the short duration of Pi2 packets (10–15 min), combined with the low spatial and temporal resolution of measurements both on the ground and in the magnetotail make it very difficult to understand Pi2 generation based on measurements alone. Few simulation studies have been carried out to investigate Pi2 generation. *Lee and Lysak* [1999] used an MHD simulation with ideal dipole to investigate Pi2 generation in the plasmasphere as a result of a compressional disturbance propagating Earthward in the magnetotail. More recently, *Fujita and Tanaka* [2013] used a global MHD simulation to investigate the TR and PVR generation mechanisms for Pi2. The authors of that study found that their simulation results showed compressional waves generated at the inner edge of the plasma sheet that would then be trapped in the inner magnetosphere, consistent with the PVR mechanism for Pi2 generation. They also concluded that if the Alfvén waves were properly reflected by the ionosphere, the TR Pi2 would be established. A recent event study of a substorm on 14 September 2004, simulated by using the UCLA 3-D global magnetohydrodynamic (MHD) model [*Ream et al.*, 2013], examined whether flow bursts generate Pi2 period fluctuations in the tail as they travel earthward from the

reconnection region. The authors showed that inside $\sim -12\ R_E$ the earthward velocity, magnetic field, and pressure all fluctuate at Pi2 frequencies when a flow channel is present. In this paper, we follow on the results of *Ream et al.* [2013] and use both the Lyon-Fedder-Mobarry (LFM) and the UCLA 3-D global MHD simulations to further study the Pi2 pulsations observed during this substorm event. We investigate how the fluctuations generated by fast flows in the tail propagate through the braking region into the inner magnetosphere. We also investigate the effects of different ionospheric models used in the simulations on the propagation of the perturbations. It has been shown that convection in the tail is strongly linked to the ionospheric conductance [*Coroniti and Kennel*, 1973]. If the perturbations are being carried by the fast flows from the tail into the inner magnetosphere, the magnitude of the ionospheric conductance should strongly affect how far earthward the perturbations can propagate. The global MHD simulations that we use lack a plasmasphere, so we are not able to investigate models in which the plasmasphere's response is important. We focus on the disturbance in the magnetotail and near-Earth plasma sheet and investigate whether the Pi2 period perturbations are contained within the fast flow channels or if the flow channels carry a broadband signal that would have to be filtered by some additional mechanism in the inner magnetosphere.

The paper is organized as follows: Satellite and ground-based observations for 14 September 2004 are described in section 2. In section 3 we describe the MHD simulations, and in section 4 we compare the results from both the UCLA and LFM models to the observations. In section 5, we identify and compare the Pi2 period perturbations in the simulations and discuss their relation to the ionospheric parameters and dipolarization fronts. A summary of our conclusions is given in section 6.

2. Observations

The substorm selected for this case study occurred on 14 September 2004. Observations of this event have previously been presented by *Cao et al.* [2008, 2012] and *Ream et al.* [2013] and are shown for the interval from 1700 to 1900 UT in Figure 1. The panels from top to bottom show the *AL* index [*Davis and Sugiura*, 1966] (Figure 1a), B_H from the Urumqi magnetometer (northwest China; 43.80° latitude, 87.70° longitude) (Figure 1b), δB_H filtered to Pi2 frequencies (Figure 1c), and magnetic field observations from the Double Star (TC1) satellite located in the plasma sheet at $(-10.2, -1.6, 1.2)\ R_E$ GSM (Figure 1d).

Based on the *AL* index (Figure 1a), there is an interval of moderate activity ($AL < -200$ nT) and variable convection that begins at ~1715 UT and lasts for ~1 h. At ~1815 UT *AL* recovers slightly before dropping again at 1827 UT. The minimum of −857 nT occurs at 1844 UT.

At the time of substorm onset (1822 UT), the ground station is situated at ~0230 MLT. Although this station is not ideally located to observe the substorm, it is the only magnetometer available for the event with high enough resolution to observe Pi2 pulsations. The observations have been band-pass filtered to 6–25 mHz (Figure 1c) to identify the Pi2 pulsations. Fluctuations in the *H* component begin at ~1822 UT and are broken up into packets. The first packet, and the one with the largest amplitude, begins at 1822 UT and continues for ~10 min. The period of the pulsations is between 60 and 90 s.

There is a discrepancy of ~5 min between the Pi2 onset in the Urumqi magnetometer measurements (1822 UT) and the main decrease in the *AL* index (1827 UT). This discrepancy may be due to the poor ground coverage in the MLT region where the substorm was located. However, it has been shown by *Hsu et al.* [2012] that it is not uncommon for Pi2 onset to precede substorm onset determined using the *AL* index by several minutes.

Auroral observations from the IMAGE spacecraft (not shown) [*Mende et al.*, 2001] show a full auroral oval remaining from a previous substorm which occurred at ~1520 UT. A bright spot begins to form in the equatorward oval at ~1814 UT then remains stagnant for several minutes before brightening further and breaking up between 1822 and 1825 UT. Based on the agreement between the timing for Pi2 onset and auroral breakup, we identify 1822 UT as substorm onset. *Cao et al.* [2012] argues that the auroral streamers observed in the IMAGE satellite auroral data between ~1801 and ~1820 UT give evidence of earthward flows prior to substorm onset.

In addition to the ground-based and auroral observations, plasma sheet observations are available from the Double Star (TC1) satellite. Data from the TC1 Fluxgate Magnetometer (FGM) [*Carr et al.*, 2005] are shown in Figure 1d. The traces show B_x (black), B_y (red), and B_z (green) in nanotesla in GSM coordinates. Based on the magnetic field measurements, the satellite is near the edge of the plasma sheet during the interval leading

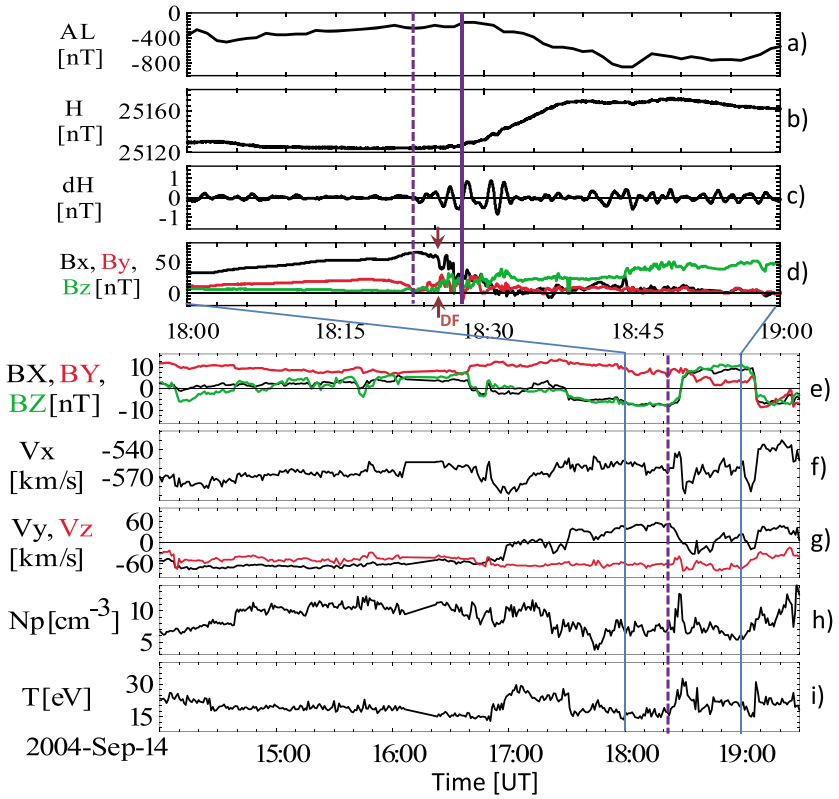

Figure 1. Ground and satellite observations for 14 September, 2004. (a) The 1 min *AL* index from the OMNI database, (b) B_H from the ground magnetometer in Urumqi, China, (c) δB_H for the Urumqi observations filtered to Pi2 frequencies, (d) Double Star (TC1) magnetic field observations in the plasma sheet, B_x (black), B_y (red), and B_z (green) in nanotesla in GSM coordinates for the interval 1700–1900 UT. Geotail solar wind measurements in GSM coordinates for the interval 1400–1930 UT used for input in the MHD simulations are shown in Figures 1e and 1f. (e) Magnetic field B_x (black), B_y (red), and B_z (green) (black) (nT), (f) Solar wind velocity v_x, (g) Solar wind velocity v_y (black), v_z (red) (km/s), (h) density (cc^{-3}), and (i) ion temperature (eV). The dashed purple line marks the time of Pi2 onset at Urumqi. Solid purple line marks *AL* substorm onset. Solid blue lines mark the start and stop times for the interval shown in Figures 1a–1d. Arrows mark DF in the observations.

up to onset and within the plasma sheet during the expansion and recovery phases. TC1 observes a DF at ~1825 UT that is preceded by Pi2 period fluctuations in B_z by several minutes. We will come back to this point in section 4. This suggests a link between the two phenomena and is consistent with models of Pi2 generation in the tail [e.g., *Kepko et al.*, 2001].

At the time of the substorm Geotail was located in the solar wind just outside the bow shock at ~(25, 17, −2) R_E GSM. Solar wind measurements from Geotail, propagated to the bow shock, are also shown in Figure 1. The panels show magnetic field (nT) (Figure 1e), solar wind velocity v_x (km/s) (Figure 1f), solar wind velocity v_y and v_z (km/s) (Figure 1g), density (cm^3) (Figure 1h), and temperature (eV) (Figure 1i). Between ~1640 and 1720 UT B_y dominates in the solar wind. The solar wind magnetic field turns southward at 1707 UT, just over an hour before substorm onset. There is a northward turning just after 1830 UT, a few minutes after substorm onset.

3. Simulation

To investigate the propagation of Pi2 pulsations, we have simulated this substorm using both the LFM and the UCLA 3-D global MHD models. The goal in using two models is to determine whether the fluctuations observed in the simulation are an artifact of the numerical methods used in the models or if they are indicative of a more general response to solar wind driving that is independent of the details of the models.

There are several differences between the two models in both the numerical methods used and in the general setup. A detailed description of the UCLA model can be found in *Raeder et al.* [1998], *El-Alaoui* [2001], and *El-Alaoui et al.* [2009]. A detailed description of the LFM model can be found in *Lyon et al.* [2004].

One of the major differences is in the gridding. The UCLA model uses a stretched Cartesian grid which is optimized to keep high spatial resolution in the plasma sheet, specifically in the near-Earth region. LFM uses a nonorthogonal, stretched spherical grid. Grid spacing is set up to keep resolution high in regions of interest such as the dayside magnetosphere, the magnetopause, and the plasma sheet. The grid resolution in the tail region between −5 and −20 R_E is ∼0.17 to 0.30 R_E in both models for the simulations used in this investigation.

Additionally, the treatment of the boundary conditions differs between the two models. For the inner boundary, both simulations include ionospheric conductance models based on the formula presented by *Robinson et al.* [1987], which accounts ionization arising from both solar EUV and auroral precipitation to solve for the Hall and Pedersen conductances in the ionosphere. However, the auroral contribution is calculated differently in each of the models. To account for the discrete auroral contribution to the conductance, the UCLA model uses the precipitation model proposed by *Knight* [1973] and *Lyons et al.* [1979] to calculate the energy and energy flux of precipitating electrons that have been accelerated by a parallel potential drop (see also *Fridman and Lemaire* [1980]). The model assumes steady state and incorporates precipitation only in regions of upward field-aligned currents. To account for the diffuse auroral contribution, following *Kennel and Petschek* [1966], the ionospheric model used in the UCLA simulation assumes that the electron distributions become isotropic at a radial distance of 3.7 R_E.

The ionospheric model used in LFM has been described in detail in *Fedder et al.* [1995] and *Wiltberger et al.* [2009], so we only give a brief description here. The model calculates the number flux and mean energy of the precipitating electrons by first calculating the initial energy and thermal flux using the sound speed and the plasma density at the inner boundary of the MHD region in the simulation. Constants are used in the equations for number flux and mean energy to scale the precipitation energy to reasonable values in order to obtain results for the conductances that are consistent with measurements [*Slinker et al.*, 1999]. Next, following work by *Chiu and Cornwall* [1980] and *Chiu et al.* [1981], the parallel potential drop along field lines between the inner boundary of the simulation grid and the ionosphere is calculated. A scaling factor is used in this step to include an effective resistivity to the field-aligned current that is taken to be 5 times larger for upward current than for downward current. This accounts for the stronger electric field required to draw "hot" electrons from the magnetosphere into the ionosphere than that required to draw "cold" electrons out of the ionosphere. Finally, the effects of the field-aligned potential on the electron flux in a geomagnetic mirror field are accounted for based on work by *Owens and Fedder* [1978].

The sunward outer boundary in the simulations is set by using solar wind observations from Geotail (Figures 1e–1i). In both simulations the solar wind magnetic field propagates as a plane wave from the sunward boundary. Since the magnetic field is divergence-free, the normal component of the solar wind magnetic field, B_n, is set to a constant in both models. The UCLA model uses a minimum variance technique to identify B_n, which is then set to a constant for the entire simulation interval [*El-Alaoui*, 2001]. The LFM model assumes that $B_{x_{SM}} = 0$.

To ensure that we have a uniform time base for comparison between the simulations and the observations, we line up the times when the northward turning in the solar wind reaches the bow shock position (12.5 R_E). The northward turning occurs at 1832 UT in the observations. Lining up the structure in the simulations resulted in a temporal shift of 4 min in the UCLA results, and 18 min in the LFM. These time shifts ensure that features discussed in the simulations and satellite observations have the same solar wind driver. Throughout this paper we will discuss the simulation results based on the timing relative to the observations.

4. Simulation Results

Cross-field flows are fastest near the center of the plasma sheet. In order to identify the perturbations associated with the fast flows, we must first determine the location of the plasma sheet in the simulation results. We identify the plasma sheet by selecting the surface of minimum $|B_x|$ in GSM coordinates. Since the UCLA model is set up on a Cartesian grid we simply select the z location for each (x, y) pair that has the minimum $|B_x|$ value in the region $|z| < 8\ R_E$. Due to the nature of the grid in the LFM model we cannot use the same technique to identify the plasma sheet as was used for the UCLA model. Instead, we select the grid points that have $|B_x| < 2.5$ nT and $4 > z > -8\ R_E$. The selected points are then projected onto a plane, and linear interpolation is used to plot them on a regular grid with a grid spacing of 0.2 R_E in both the x and y directions. The average z value is found for each point on the grid to determine the location of the plasma sheet. In the simulation results the plasma sheet is displaced from the geomagnetic equator by several R_E at distances

greater than 15 R_E down tail. The large span in z included in the selection criterion accounts for that displacement and allows for identification of the plasma sheet as far tailward as −40 R_E. We find that, in both simulations, the plasma sheet is located between $z = 2$ and $z = 0$ R_E in the region $-12 \leq x \leq 0$ R_E then begins to tilt in the $-z$ direction so it is located at $z \approx -7$ R_E at $x = -30$ R_E.

Snapshots of the plasma properties at the location of the plasma sheet from the simulations are shown in Figure 2. The top panels show results from the UCLA model, and the bottom panels show results from the LFM model, every minute between 1821 and 1826 UT. The background color shows B_z between 50 and −50 nT. The green color marks $-0.15 \leq B_z \leq 0.15$ nT to show approximate locations for the reconnection regions in the plasma sheet. Black arrows show the velocity in the plane, and gray contours show thermal pressure. In most cases there is a stagnation point in the flows at or near the green regions where B_z=0, supporting the assumption that reconnection is occurring in those regions.

There are several similarities in the global configurations in the two simulations. Through most of the substorm intervals, the reconnecting regions (green in Figure 2) in both simulations are located between −20 and −25 R_E. Reconnection in the UCLA results is more patchy than in LFM, probably because the current-dependent anomalous resistivity in the UCLA model allows for reconnection in more localized regions. Most of the fast flows from the reconnection regions in both models are slowed and diverted before reaching −12 R_E. As a result of this diversion, the flow channels that penetrate farther earthward are pinched into azimuthally thin structures, in agreement with observations of narrow channels of fast plasma flows in the tail. The diversion itself is due to vorticity from earlier flow channels and the formation of a secondary minimum in B_z 2–5 R_E earthward of the reconnecting regions. The vorticity observed in the simulation results is similar to that presented in previous MHD studies of flow channels [e.g., *El-Alaoui et al.*, 2009; *Birn et al.*, 2011; *El-Alaoui et al.*, 2013]. An example of the secondary minimum in B_z can be found in the 1821 UT snapshots in Figure 2 at the locations marked by the light blue triangles.

The flow channel in the UCLA results that agrees in timing and location with the appearance of dipolarization at the TC1 spacecraft is fairly isolated and forms near midnight (0045 MLT). There are other DFs that form around the same time as the DF that agrees with the TC1 observations, but they are located at different local times so they would not have been observed by TC1. The flow channel in the LFM results is also located very close to midnight between 0045 and 0100 MLT, but there is also a very strong flow channel that forms earlier, just after 1800 UT and persists for over 20 min just to the dusk side of midnight between 2300 MLT and midnight. Thus, the LFM flow channel that agrees with the TC1 observations is not as isolated, spatially or temporally, as is the corresponding flow channel in the UCLA simulation. The dark green cross in each panel of Figure 2 marks the location of TC1 and the large dark blue arrows mark the earthward edge of the flow channel that corresponds to the observations. The flow channels that correspond to the Double Star observations in each simulation occur at similar times, reaching −8 R_E at ∼1826 UT, close to the time of substorm onset. Both simulations did a reasonable job reproducing DFs at the location of the TC1 observations. However, with the sparse observations available for this event it is difficult to determine how localized the DF was for this event, so we cannot determine whether one simulation or the other more accurately recreated the DF. In general, the DFs in the UCLA model look more like the medium-scale flows presented by *Henderson* [2012].

To study the changes in the plasma sheet leading up to substorm onset in the simulations, we have taken snapshots at each time step and subtracted values of the parameters at the previous time step (δt=30 s). Figure 3 shows the results of the differencing for the snapshots shown in Figure 2. The background color is δB_z and the arrows show δv in the plane. The gray contours show the total thermal pressure giving us a reference for where the DF has formed in the simulation. The DF appears as an enhancement in δB_z that is both preceded and followed by a depression in δB_z. This structure is accompanied by an enhancement in the earthward flow.

By plotting the perturbations in the plasma sheet in this manner we can see that the flow channel and associated DF that forms in the UCLA results is a very well defined structure that forms near 20 R_E and travels earthward, reaching ∼8 R_E at 1826 UT. We can also see that the flow channel that formed in the LFM simulation around 1800 UT is relatively steady. There is a set of DFs that form in the LFM simulation and travel earthward with the flow early on, but after ∼1815 UT there is relatively little change associated with the flow channel until 1820 UT when the flow channel widens and a new DF forms. As was noted above, this new DF is in the correct location to account for the observations from the Double Star (TC1) satellite in the plasma sheet and the available ground-based magnetometer. The green crosses and large blue arrows are the same as those found in Figure 2 and mark the TC1 location and closest approach of the observed DF to Earth at each time

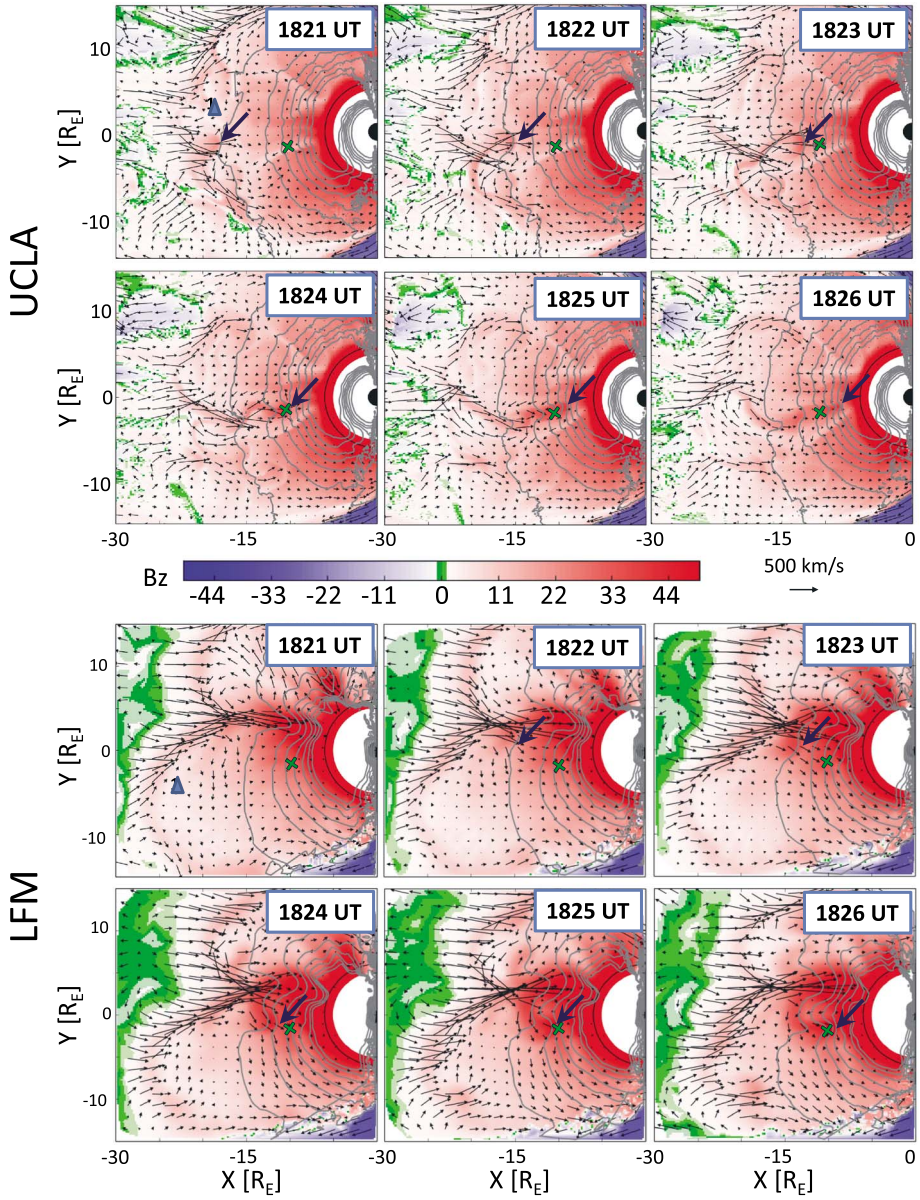

Figure 2. Plasma sheet results from the (top) UCLA and (bottom) LFM simulations for 14 September 2004. Snapshots are shown each minute between 1821 and 1826 UT. The area shown is $-30 \le x \le 0\ R_E$ and $-15 \le y \le 15\ R_E$. Background color shows B_z from −50 (blue) to 50 (red) nT with the green color marking $|B_z| < 0.15$ nT. A reference vector is shown for 500 km/s. Black arrows show the velocity in the plane and the gray contours show thermal pressure (0–4000 pPa, $\delta P = 500$ pPa). The solid black line marks the radial distance of 6 R_E. The TC1 location is marked by the dark green cross. The large blue arrow indicates the earthward edge of the DF that is consistent with TC1 observations. The blue triangle marks an example of a secondary B_z minimum a few R_E earthward of the reconnection regions. The Sun is to the right.

step. A movie of the simulated plasma sheet (UCLA, top left; LFM, top right) and the time-differenced plasma sheet (UCLA bottom left, LFM bottom right) for the event is included in the supporting information. The panels in the movie frames are laid out in the same format as the panels in Figures 2 and 3. The series of events that occur during the course of the simulation interval are similar in the two models. Reconnection begins between 1715 and 1720 UT and several flow channels form and travel earthward during the hour leading up to the substorm. Most of the activity prior to the substorm onset occurs in the dusk sector. At ~1820 UT, a flow channel with an associated DF forms and crosses the TC1 location. Several additional DFs form and travel earthward until ~1845 UT when the reconnection regions move tailward and activity in the near-Earth plasma sheet diminishes.

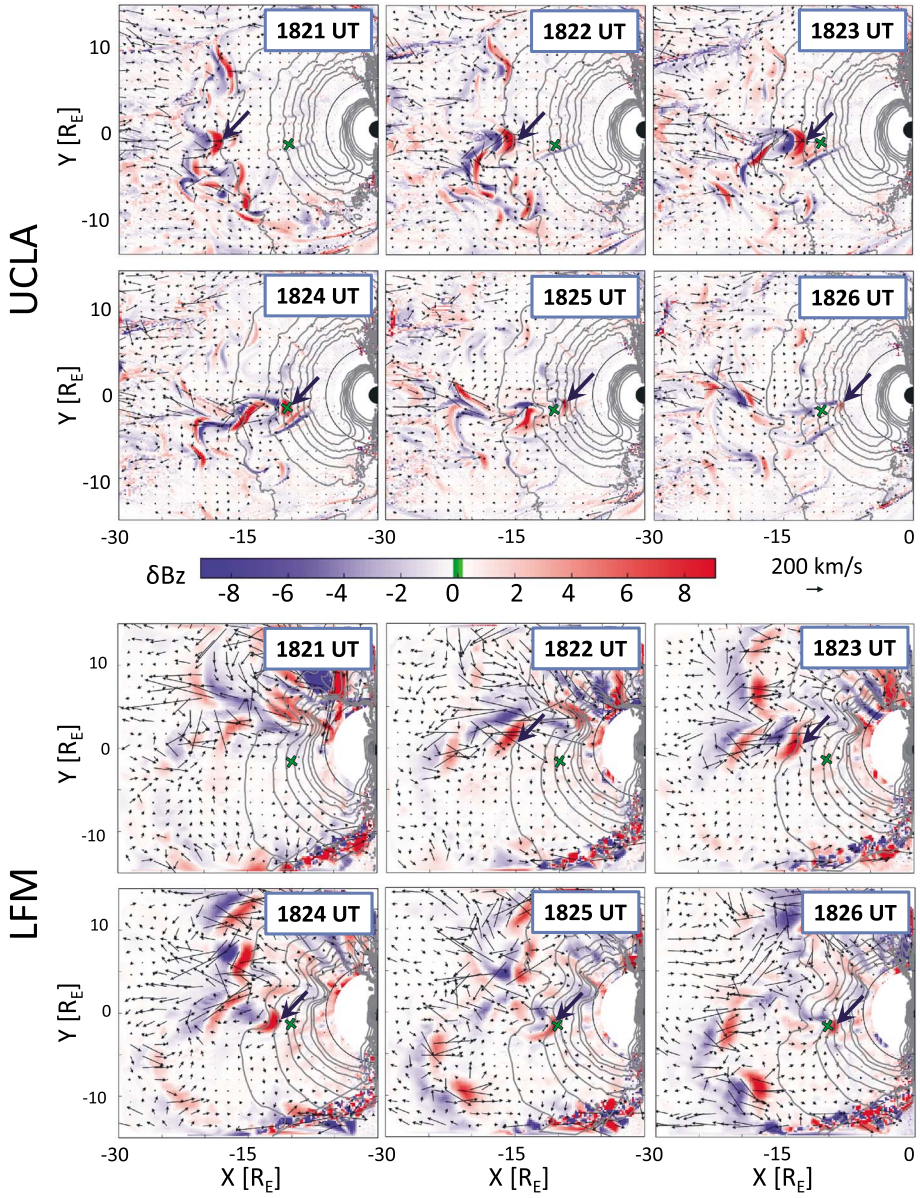

Figure 3. Time-differenced plasma sheet results for 14 September 2004 in the same format as Figure 2. The color bar shows $-10 \leq \delta B_z \leq 10$ nT and the reference vector shows $\delta v = 200$ km/s.

Figure 4 shows δB_z, filtered to Pi2 frequencies from (a) the UCLA model and (b) the LFM model at the location of the Double Star (TC1) satellite (Figure 4b), and Double Star observations (Figure 4c), along with ground Pi2 signatures (δH) (Figure 4d). In each data set there is a DF accompanied by Pi2 period perturbations. The large peak at 1825 UT in the TC1 δB_z corresponds to the DF in the observations; however, as was noted in section 2, smaller amplitude Pi2 period pulsations begin at ~1820 UT, 5 min before the DF arrives. In the UCLA trace (Figure 4a) perturbations begin at nearly the same time as the perturbations observed by TC1 and correspond to the DF indicated by the thick arrows in the top panels of Figures 2 and 3. In the LFM trace (Figure 4b) there are perturbations beginning 1753 UT which are related to the earlier, persistent, flow channel in the dusk sector. These perturbations damp out by ~1815, then a new packet forms at ~1823 UT. It is the second packet that agrees most closely in time and location with the available observations. There are also perturbations that begin around 1730 UT and just after 1750 UT in the UCLA simulation but the responsible flow channels are a very transient structures and the perturbations damp out quickly, whereas the flow channel in the LFM simulation is a persistent structure, as mentioned above, that continues to drive perturbations for more than 20 min.

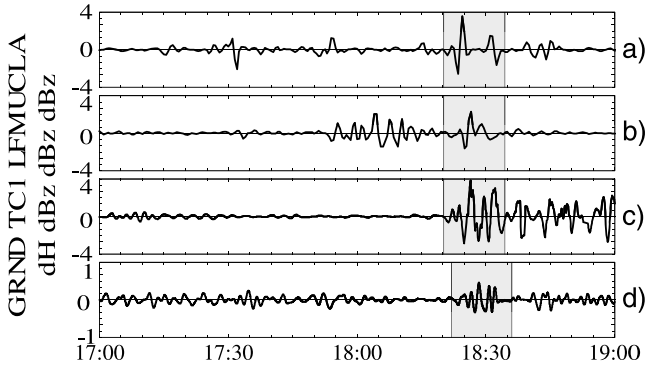

Figure 4. δB_Z band-pass filtered to 6–16 mHz for the interval 1700–1900 UT for (a) UCLA, (b) LFM simulations results near the TC1 location, and (c) TC1 observations. The gray areas indicate times when the Pi2 in the simulation correspond to the TC1 measurements. Figure 4d shows the Pi2 pulsations measured from the ground for comparison (also shown in Figure 1c.)

Although there are some obvious differences in the two simulations, each individual simulation can account for the observations available during the event. The Urumqi magnetometer was located at ~0300 MLT during the expansion phase of the substorm. In the simulations and observations available for this event the flow channel locations are within 2.5 h of the Urumqi local time. Using a selection of 48 Pi2 events that occurred when Time History of Events and Macroscale Interactions during Substorms (THEMIS) was in the inner magnetosphere, *Kwon et al.* [2012] has shown that space and ground observations of Pi2 are coherent if the satellite is within about 3 h of MLT of the ground station. *Ream et al.* [2013] showed that the pulsations observed in the UCLA simulation are coherent for ~2.5 h MLT at a radial distance of 6 R_E, in good agreement with the observational results. The upper limit of the coherence in the LFM results is 2 h MLT. Therefore, it is reasonable to assume that the flow channel observed by TC1 and the corresponding flow channels in the simulations would contribute to the fluctuations observed by the Urumqi magnetometer beginning at ~1822 UT. Although there are several flow channels that form in each of the two simulations during the substorm interval, we focus on the flow channel located closest to midnight since that structure can account for the observations available for this event. The timing for the TC1 DF also indicates that it is related to substorm onset.

The changing properties of the ionosphere in the two simulations are shown in Figure 5 for 1818 UT (disturbed interval prior to onset), 1828 UT (substorm onset), and 1838 UT (recovery phase). In general, the magnitudes of the Hall and Pedersen conductances are much higher in the UCLA simulation than in the LFM simulation. As a result the potential is much lower in the UCLA simulation than in the LFM simulation. However, the configuration and strength of the field-aligned currents are very similar in the two models throughout the growth and expansion phases of the substorm.

Large differences in the ionospheric conductance and potential can have a dramatic effect on flow patterns in the plasma sheet. If the conductance in the ionosphere becomes too large, the flows in the tail are slowed or stopped because the field-aligned currents are insufficient to support the full solar wind potential drop across the polar cap and the ionosphere is unable to return the magnetic flux to the dayside [*Coroniti and Kennel*, 1973; *Walker et al.*, 2006]. Therefore, the high conductances in the UCLA model result in very small flow velocities in the near-Earth plasma sheet, earthward of ~8 R_E. In contrast, the low conductances in the LFM results allow the plasma flows to move more freely into the inner magnetosphere. This effect can be seen in Figure 2. Comparison of the flow vectors between UCLA and LFM shows that the flow speeds in LFM are typically higher than those in the UCLA results, particularly in the fast flow channels and in the flow moving around Earth toward the dayside. Figure 2 also shows that in the region $7 < r < 10\ R_E$ the velocity in the flow channels in the UCLA results drops to $<$ 50 km/s, while in the LFM results the velocity in the flow channels is $>$ 100 km/s and only drops below 50 km/s inside of ~6.5 R_E. In the LFM results, the flow-braking region is more smeared out in radial distance and the inner edge is located closer to Earth than in the UCLA results.

Figure 6 shows field line traces taken from latitudes of −80° to −60° at 0100 MLT for (1) UCLA and (2) LFM. Panels a and b show the Pedersen conductance and the field-aligned currents for the respective simulations at 1828 UT, just after substorm onset. The numbered locations in each plot show where the foot points of the field line traces are located in the ionosphere. The top row in panels c–e show the field lines in x–z with

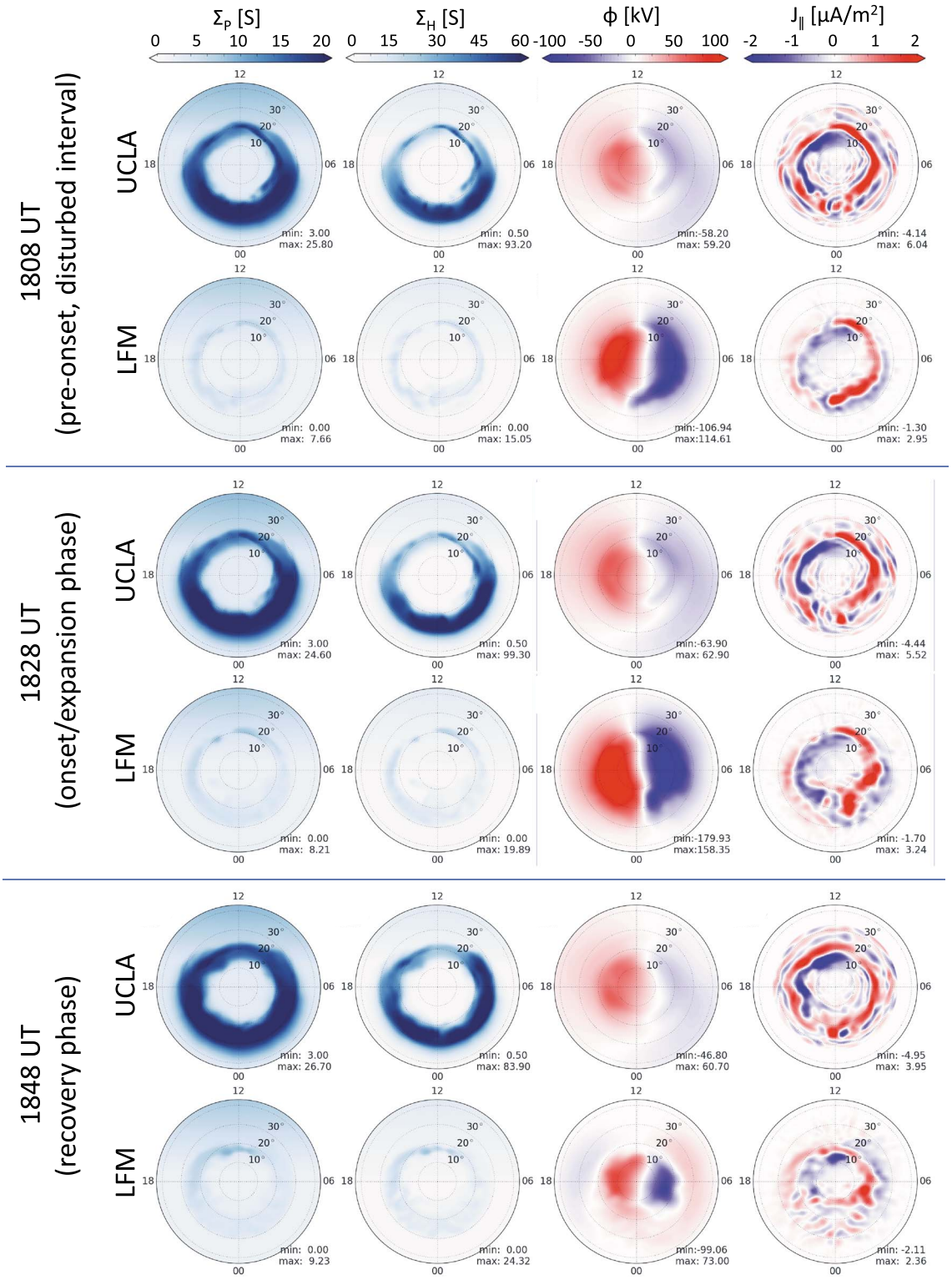

Figure 5. Ionospheric plots for (a) 1808 UT, (b) 1828 UT, and (c) 1848 UT. The top row in each panel shows UCLA results and the bottom row shows LFM results. Columns from left to right show Pedersen conductance (S), Hall conductance (S), Potential (kV), and parallel current [$\mu A/m^2$].

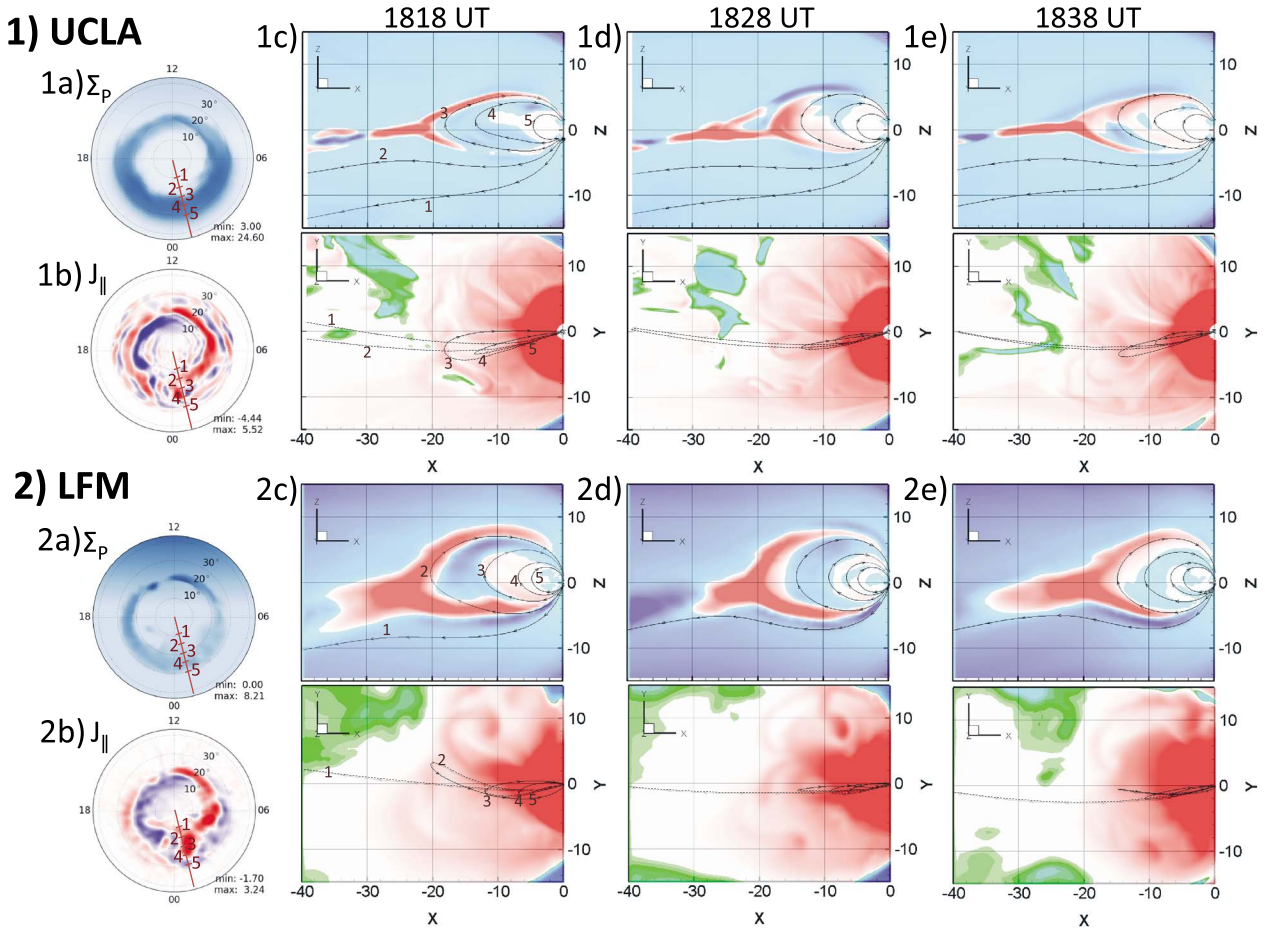

Figure 6. Results of field line traces from (1) UCLA and (2) LFM for times before, during, and after substorm onset. (a) Pedersen conductance and (b) parallel currents at 1828 UT. Field lines with foot points at the numbered locations in Figures 6a and 6b are shown at (c) 1818 UT, (d) 1828 UT, and (e) 1838 UT. The top row in each panel shows an $x-z$ view of the field lines with v_x shown in the color background. The bottom row shows an $x-y$ view of the same field lines with B_z in the background. Field lines south of the geomagnetic equator are dashed. The numbers indicate which foot point the field line corresponds to in panels a and b.

v_x at $y=0$ plotted in color. Red shows velocity in the positive x direction and blue shows velocity in the negative x direction. The bottom row shows the same field lines in $x-y$ with B_z in color (red, positive; blue, negative). Figures 6-1c and 6-2c show a snapshot at 1818 UT during the disturbed interval prior to substorm onset. Figures 6-1d and 6-2d show a snapshot at 1828 UT, about 1 min after onset during the expansion phase. Finally, Figures 6-1e and 6-2e show a snapshot at 1838 UT which is in the recovery phase of the substorm.

Although both simulations show plasma sheet thinning, in general, the plasma sheet is thicker in the LFM model than in the UCLA model, which may be due to the resistivity being purely numerical in LFM while UCLA includes an anomalous resistivity term in Ohm's law. The field lines in the UCLA model are more stretched than those in the LFM results for latitudes >65°. Additionally, the field lines become open between 70° and 75° latitude in the UCLA model. In the LFM model field lines become open between 75° and 80° latitude. Figure 6 shows that in both simulations the field lines are dragged duskward at radial distances greater than ~6 R_E. The same is true when we map field lines from the local time of Urumqi into the plasma sheet. We find that they are dragged toward midnight in the plasma sheet with the displacement becoming larger at higher latitudes. Therefore, even though the substorm is occurring near midnight the field lines map from a local time at the equator to an ionospheric location farther into the dawn sector, close to the Urumqi location.

To look at the fluctuations associated with the flow channels observed in the simulations in association with substorm onset, we first identified the path of the flows in each of the simulations by selecting the points in the simulation where the flows exceeded 250 km/s in the interval during which the flow was observed. We then calculated the average y location for each x location in that region to find the average center of the flow channel as it propagated earthward. This effectively traces the path of the flow channel marked by the

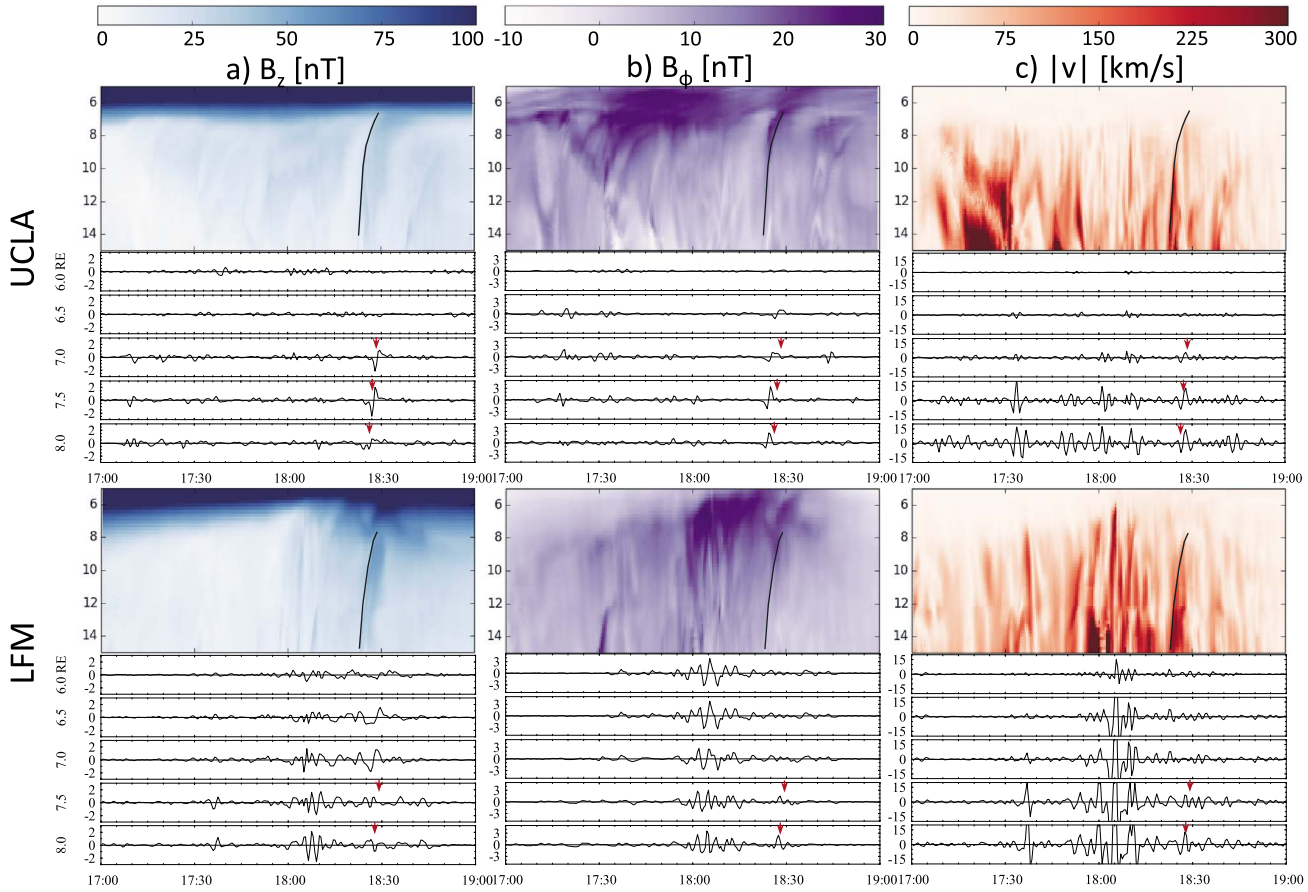

Figure 7. Average quantities and perturbations for 15 min of MLT on the dusk half of the flow channels that agree with the TC1 measurements as identified in Figures 2 and 3 for (top) UCLA and (bottom) LFM between 1700 and 1900 UT. From left to right, color plots show the average quantities B_z, B_ϕ, and $|v|$ plotted versus radial distance from Earth and time. The black line shows the path of the DF through the system determined using B_z and copied onto the other panels. The line plots show cuts between 6 and 8 R_E for each of the components band-pass filtered to 6–16 mHz (the portion of the Pi2 band that can be resolved in the simulations). Red arrows indicate the DF crossing time at each radial distance.

large blue arrows in Figures 2 and 3. To identify the fluctuations in the magnetic field (radial and azimuthal components), velocity, and pressure in the flow channel, we averaged across 15 min of MLT on the dawn half of the flow channel at fixed radial distances and plotted the results as a function of radial distance and time. Only the dawn half of the flow channel was selected because the fluctuations in δB_ϕ are ideally antisymmetric about the center of the flow channel.

The magnetic field and velocity fluctuations for the interval 1700–1800 UT in the region 5–15 R_E are plotted in Figure 7. The columns show B_z (Figure 7a), B_ϕ (Figure 7b), and $|v|$ (Figure 7c) for UCLA (top) and LFM (bottom). B_z and $|v|$ were taken at the center of the plasma sheet while B_ϕ was taken 1.5 R_E above the center of the plasma sheet. Color plots show the total value for each of the three components with the path of the DF indicated by the solid black line. The path of the DF was determined by using the beginning of the enhancement in the total B_z in Figure 7a. The line plots show radial cuts at 6.0, 6.5, 7.0, 7.5, and 8.0 R_E band-pass filtered to 6–16 mHz (16 mHz is the Nyquist frequency for the simulation output). Red arrows indicate the crossing time of the DF. There are Pi2 period perturbations in B_z, B_ϕ, and $|v|$ in both simulations; however, there is also a significant broadband signal in B_z. The broadband signal is more prominent in the UCLA simulation than in LFM. With the limited observations available in the tail for this event, it is difficult to determine whether one or the other simulation has more accurately reproduced the event itself. However, in general, both models show Pi2 period perturbations associated with the flow channels that form in the plasma sheet and reproduce TC1 observations, even though the models use dramatically different grids and numerical methods to solve the set of MHD equations. As a result, we believe that the modeled Pi2 period pulsations are inherent in the MHD description of the system and are independent of the initial setup and the numerical methods used.

5. Discussion

By using MHD simulations to address the question of how Pi2 period perturbations propagate through the near-Earth plasma sheet, we are able to get a global view of the system. By using two different simulations to study the same event, we are able to ascertain those features of Pi2 propagation that are robust and those that reflect idiosyncrasies of the simulations themselves.

Throughout the magnetotail, flow velocities in the LFM simulation are typically higher than those in the UCLA simulation (see Figure 2). Because the flows do not propagate as far earthward in the UCLA simulation, the perturbations carried by the flow channels are also not able to penetrate as far into the inner magnetosphere. This effect can be seen in the line plots in Figure 7. Fluctuations in the flow velocity and magnetic field diminish to noise levels before reaching 6.5 R_E in the UCLA results, while in the LFM results the fluctuations are still evident at 6.0 R_E. This is likely a result of the differences in the ionospheric conductance models used in the simulations (see section 4). Figure 5 shows very clearly that the magnitudes of the conductances in the UCLA model are much higher than those in the LFM model. The high Pedersen conductance in the UCLA simulation effectively stops the earthward flow in the tail inside of ~7.5 R_E [*Coroniti and Kennel*, 1973; *Walker et al.*, 2006]. In contrast, the flow in the LFM simulation is able to penetrate much farther earthward; in some cases as far as 5 R_E.

In order to confirm our interpretation of the effects of the different Pedersen conductances in the two models, we compare two additional simulations run with the same model, in this case the UCLA model, with different ionospheric conductances. Only the UCLA model was used in order to isolate the effects of the conductance. Both simulations were driven by constant idealized solar wind conditions. Solar wind conditions were $v_x = 450$ km/s, $n = 10$ cm^{-3}, and $P = 20$ pPa. The IMF was set to a constant −5 nT for the entire 4 h simulation interval. The only difference in the two simulations is in the Pedersen conductance (Σ_P). For Run 1 $\Sigma_P = 6$ S. For Run 2 $\Sigma_P = 20$ S. The results of the simulations can be seen in Figure 8. The figure shows that in Run 1 fast flow channels have formed by $t = 3600$ s, 1 h into the simulation. Fast flows continue to form and propagate earthward until $t = 10800$ s. In Run 2 we also see that the flow channels form in the simulation by $t = 3600$ s. However, by $t = 7200$ s those flows have died out and no new flow channels are propagating into the near-Earth region. In general, the larger the Pedersen conductance, the fewer the flow channels. Those that develop for large Σ_P stop further out in the tail. Run 1, with low Σ_P gives results similar to the LFM results where the Pedersen conductance stays low throughout the event, and fast flows continue to form and propagate into the near-Earth region well into the recovery phase. Run 2, on the other hand, gives results similar to those found in the UCLA simulation for the current event study. Flow channels form early on in the simulation, but as the event progresses, the Pedersen conductance increases and fast flows are stopped further out in the magnetotail. There is also a very large gradient that forms in the magnetic field which can be seen in Figures 8e and 8f. This is similar to the magnetic field gradient that forms in the UCLA model (see Figure 2). The ionospheric results for Runs 1 and 2 also correspond to the LFM and UCLA results, respectively, for the 14 September event. In Run 1, with low Pedersen conductance, the potential gets very large, with $\Delta\Phi$ exceeding 150 keV, similar to the values seen in the LFM simulation. In Run 2, with high Pedersen conductance, $\Delta\Phi$ stays well below 100 keV throughout the simulation, similar to the UCLA results for 14 September. Since the only difference between the two runs is the magnitude of the Pedersen conductance, it is reasonable to conclude that the conductance is responsible for the differences in the magnetotail dynamics. This, along with the similarities between the simulations mentioned above, suggests that the Pedersen conductance is also responsible for differences between the UCLA and LFM results for the current event study.

Figure 9 shows the magnitude of $\mathbf{v} \times \mathbf{B}$ at the location of the flow channel for UCLA (top) and LFM (bottom) in the same format as the color panels in Figure 7. The flux transport in the UCLA model falls to very low values between 6 and 7 R_E, near the inner edge of the plasma sheet. In the LFM model the flux transport stays relatively high across the inner edge of the plasma sheet. This difference in the flux transport is due primarily to line tying, but the pressure gradients in the two simulations also play a role in how far earthward the flows are able to penetrate. The largest pressure gradients are closer to Earth in the LFM simulation than in the UCLA simulation. As a result, the flow speeds decrease at larger radial distance in the UCLA model so the flow channels are not able to penetrate as far earthward as those in the LFM simulation.

The two simulations also differ in the thickness of the plasma sheet (see Figure 6) and in the size and duration of the flow channels that form in the plasma sheet (see Figures 2 and 3). Given these differences, when we look at the perturbations generated in the flow channels observed in the simulations near the time of substorm

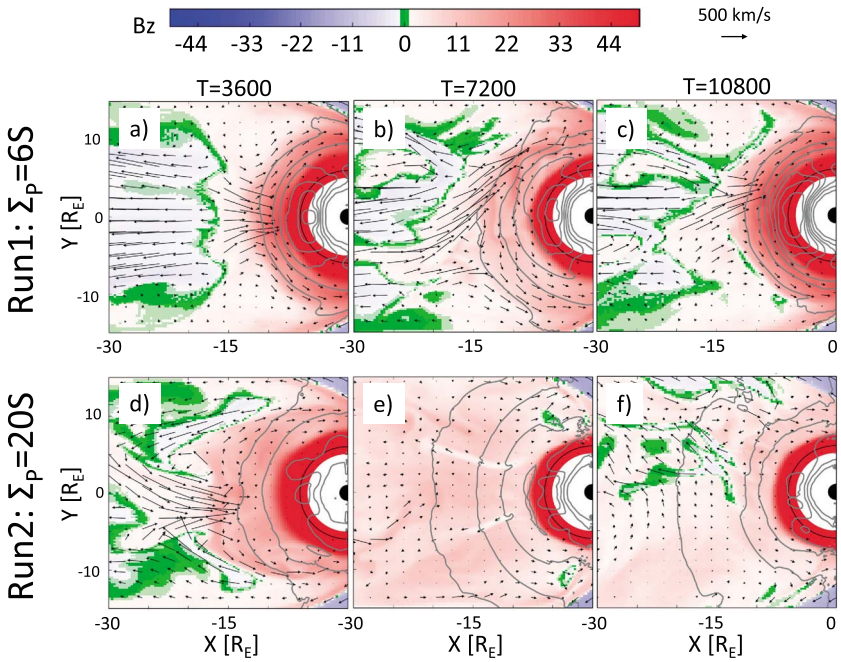

Figure 8. Simulation results from (a–c) Run 1 ($\Sigma_P = 6$ S) and (d–f) Run 2 ($\Sigma_P = 20$ S). Simulation times from left to right are $t = 3600$, 7200, and 10,800 for each simulation. Background color shows B_z. Arrows show the velocity in the plane.

onset we see that Pi2 period fluctuations are being generated in both simulations in the same way. Perturbations in B_z develop with the flow channel and the DF that forms at the earthward edge of the flow channel. *Ream et al.* [2013] showed that once the flow channel reaches $\sim -12\ R_E$, the frequency of the perturbations is within the Pi2 spectrum. The fact that the frequency of the perturbations increases as the flow channel propagates earthward supports the transient response (TR) model for Pi2 generation. Pi2 period fluctuations also develop in B_y in association with the vortices that form on either side of the flow channel, generating field-aligned currents, in support of the inertial current (IC) mechanism for Pi2 generation that is included in the bursty flow model [*Kepko et al.*, 2001; *Keiling et al.*, 2009; *Ream et al.*, 2013]. Because the period for the TR fluctuations depends on the Alfvén transit time, and both simulations have similar results for the lengths of the field lines, density and magnetic field magnitudes tailward of $\sim -7\ R_E$, both simulations exhibit similar periods

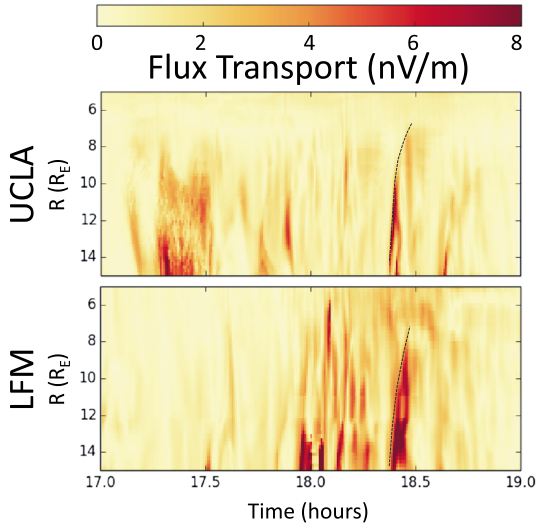

Figure 9. The flux transport $|\mathbf{v} \times \mathbf{B}|$ plotted in the same format as the color panels in Figure 7 for (top) UCLA and (bottom) LFM.

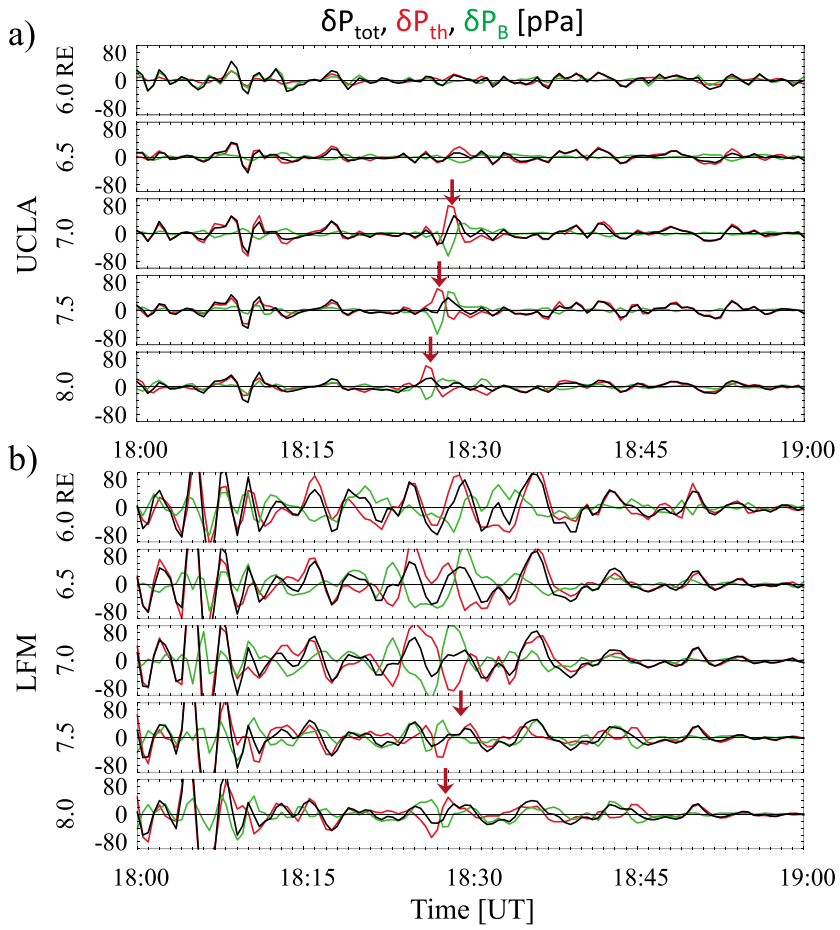

Figure 10. Pressure perturbations in the dusk half of the flow channel plotted in the same format as the line plots in Figure 7 for the interval 1800–1900 UT. Traces show δP_{total} (black), δP_{th} (red), and δP_{mag} (green) for (a) UCLA and (b) LFM.

related to the flow channels at substorm onset in that region. In the UCLA model, earthward of $-7\ R_E$ line tying damps the Earthward propagation of the disturbance. However, in the LFM model the perturbations are able to propagate much farther earthward, so the simulation results look very different in that region. However, to verify that the mechanism for Pi2 generation in the simulation is, in fact, the transient response mechanism, additional work is required. We need to model an additional event where there are enough ground observations to validate the ionosphere results and determine whether there are Pi2 period fluctuations in the ionosphere that map to the flow channels in the plasma sheet. This work is currently underway.

In both simulations the braking region lies in the region $-8 > x > -6\ R_E$ consistent with the source region for Pi2 period compressional waves identified by *Uozumi et al.* [2007]. As the flow channel and its associated DF travel through the braking region and approach the inner edge of the plasma sheet the perturbations begin to travel ahead of the DF. This effect is most evident in B_ϕ (Figure 7b) where the separation between the beginning of the perturbations and the red arrow marking the crossing time of the DF gets larger as the disturbance propagates earthward. The separation of the DF and the Pi2 period fluctuations in the braking region supports the idea proposed by *Kepko et al.* [2001], that a compressional wave traveling ahead of the DF into the inner magnetosphere could generate directly driven (DD) Pi2 pulsations at middle to low latitudes on the ground. As the compressional wave travels earthward it couples to an Alfvén wave and is transported into the ionosphere where it can be observed by magnetometers on the ground [*Uozumi et al.*, 2009, 2011].

Figure 10 shows the perturbations in the pressure for the interval 1800–1900 UT for (a) UCLA and (b) LFM. The traces show total pressure (black), thermal pressure (red), and magnetic pressure (green) at 6.0, 6.5, 7.0, 7.5, and 8.0 R_E associated with the flow channel identified in Figure 2. The red arrow marks the time of the DF crossing at each radial distance. In both simulations, the fluctuations associated with the DF show a

mixed mode compressional wave with the thermal and magnetic pressure nearly out of phase and significant fluctuations in the total pressure. This agrees well with observations of magnetotail Pi2 by *Nakamizo and Iijima* [2003], which showed that the thermal and magnetic pressure fluctuations associated with the Pi2 fluctuations were out of phase. The pressure fluctuations (magnetic, thermal, and total) in LFM and UCLA have about the same amplitude at 7.5 and 8.0 R_E; however, at 7.0 R_E the amplitude of the pressure fluctuations in LFM start to get larger while the pressure fluctuations in the UCLA results do not. Pressure perturbations travel farther earthward in the LFM model, and the oscillations become very large at radial distances smaller than 7.5 R_E. Meanwhile, pressure perturbations in the UCLA model decay earthward of ~7.0 R_E. As noted above, this is most likely an effect of the differences in the conductances between the two models. The line tying in the UCLA model is so strong that the flow perturbations are not able to propagate earthward of 7.0 R_E. Based on the pressure perturbations shown in Figure 10, the compressional wave propagates more easily into the inner magnetosphere in the LFM model than in the UCLA model. However, as mentioned above, based on the line plots in Figure 7, both simulations show a compressional wave traveling ahead of the DF as it slows in the braking region.

6. Summary

We have used two different 3-D global MHD models, UCLA and LFM, to model the generation and propagation of Pi2 pulsations during a substorm event on 14 September 2004. Although we are unable to rule out plasmaspheric eigenmodes as a source for Pi2 pulsations observed on the ground, the simulations demonstrate that, in some cases, fast flows in the plasma sheet are directly responsible for generating Pi2 pulsations. When we focus on the flow channel that forms around the time of substorm onset in the simulations, we observe Pi2 period perturbations inside $\sim -12\ R_E$ in the magnetic field, velocity, and pressure propagating at the same speed as the DF at the earthward edge of the fast flow until it reaches the braking region in agreement with the transient response model for Pi2 [*Southwood and Stuart*, 1980; *Kepko et al.*, 2001]. However, more work is needed to verify the transient response mechanism in the simulations. Pi2 period perturbations are observed in B_y in association with the vortices that form on either side of the flow channel in support of the inertial current component of the bursty flow model. As the DF approaches the inner edge of the plasma sheet and is slowed in the braking region, the perturbations begin to travel ahead of it as a mixed mode compressional wave. These propagating compressional waves generated by the fast flows in the braking region can produce Pi2 pulsations observed on the ground as described by the bursty flow model for Pi2 generation [*Kepko and Kivelson*, 1999; *Kepko et al.*, 2001, 2004].

Although the perturbations are generated in the same way in both models, the propagation of the perturbations into the inner magnetosphere is greatly affected by the differences in the ionospheric models in the simulations. The high Pedersen conductance (~25 S) in the UCLA results causes the flow channels and the perturbations to stop propagating earthward at ~7 R_E, whereas the perturbations in the LFM results, with its maximum Pedersen conductance around 9 S, are able to propagate more easily into the inner magnetosphere.

Acknowledgments

This work was supported by NASA grant NNX09AV91G. This research was also supported in part by the NASA Graduate Student Research Program through Goddard Space Flight Center, grant NNX10AM08H. M.L. Goldstein and M. Ashour-Abdalla were supported by the Magnetospheric Multiscale project through an Interdisciplinary Science grant to the Goddard Space Flight Center and UCLA (NASA grant NNX08AO48G at UCLA). M. El-Alaoui was supported by NSF grant AGS-1265967. M.G. Kivelson was supported by NASA grant UCB/NASA NAS 5-02099. M. Wiltberger was supported by NASA grant NNX13AE39G. The National Center for Atmospheric Research is sponsored by the National Science Foundation. We would like to acknowledge high-performance computing support from Yellowstone (ark:/85065/d7wd3xhc) provided by NCAR's Computational and Information Systems Laboratory, sponsored by the National Science Foundation. Computational resources for the UCLA model were provided by the Extreme Science and Engineering Discovery Environment (XSEDE), which is supported by National Science Foundation grant OCI-1053575. All satellite and OMNI data were obtained through the Virtual Magnetospheric Observatory (VMO) (http://vmo.igpp.ucla.edu/). We acknowledge the experiment teams that acquired, processed, and provided the OMNI-included data, and J.H. King and N.E. Papitashvili of NASA/GSFC for creating the OMNI data set. Geotail magnetic field data were provided by T. Nagai, JAXA in Japan. We acknowledge C. Carr and the Double Star TC1 FGM instrument team, as well as ESA, Double Star, Center for Space Science and Applied Research, and the Chinese Academy of Sciences for Double Star data. We also acknowledge the World Data Center for Geomagnetism, Kyoto (http://wdc.kugi.kyoto-u.ac.jp/index.html) and the Geomagnetic Network of China, for Pi2 data. We thank Krishan Khurana, Tung-Shin Hsu, and Robert J. Strangeway for helpful discussions during the course of this research.

References

Angelopoulos, V., W. Baumjohann, C. F. Kennel, F. V. Coronti, M. G. Kivelson, R. Pellat, R. J. Walker, H. Luehr, and G. Paschmann (1992), Bursty bulk flows in the inner central plasma sheet, *J. Geophys. Res.*, *97*, 4027–4039, doi:10.1029/91JA02701.

Angelopoulos, V., C. F. Kennel, F. V. Coroniti, R. Pellat, M. G. Kivelson, R. J. Walker, C. T. Russell, W. Baumjohann, W. C. Feldman, and J. T. Gosling (1994), Statistical characteristics of bursty bulk flow events, *J. Geophys. Res.*, *99*, 21,257–21,280, doi:10.1029/94JA01263.

Birn, J., R. Nakamura, E. V. Panov, and M. Hesse (2011), Bursty bulk flows and dipolarization in MHD simulations of magnetotail reconnection, *J. Geophys. Res.*, *116*, A01210, doi:10.1029/2010JA016083.

Cao, X., et al. (2008), Multispacecraft and ground-based observations of substorm timing and activations: Two case studies, *J. Geophys. Res.*, *113*, A07S25, doi:10.1029/2007JA012761.

Cao, X., et al. (2012), Auroral streamers implication for the substorm progression on September 14, 2004, *Planet. Space Sci.*, *71*, 119–124, doi:10.1016/j.pss.2012.07.018.

Carr, C., et al. (2005), The Double Star magnetic field investigation: instrument design, performance and highlights of the first year's observations, *Ann. Geophys.*, *23*, 2713–2732, doi:10.5194/angeo-23-2713-2005.

Chen, L., and A. Hasegawa (1974), A theory of long-period magnetic pulsations: 2. Impulse excitation of surface eigenmode, *J. Geophys. Res.*, *79*, 1033–1037, doi:10.1029/JA079i007p01033.

Chiu, Y. T., and J. M. Cornwall (1980), Electrostatic model of a quiet auroral arc, *J. Geophys. Res.*, *85*, 543–556, doi:10.1029/JA085iA02p00543.

Chiu, Y. T., A. L. Newman, and J. M. Cornwall (1981), On the structures and mapping of auroral electrostatic potentials, *J. Geophys. Res.*, *86*, 10,029–10,037, doi:10.1029/JA086iA12p10029.

Coroniti, F. V., and C. F. Kennel (1973), Can the ionosphere regulate magnetospheric convection?, *J. Geophys. Res.*, *78*, 2837–2851, doi:10.1029/JA078i016p02837.

Davis, T. N., and M. Sugiura (1966), Auroral electrojet activity index *AE* and its universal time variations, *J. Geophys. Res.*, *71*, 785–801, doi:10.1029/JZ071i003p00785.

El-Alaoui, M. (2001), Current disruption during November 24, 1996, substorm, *J. Geophys. Res.*, *106*, 6229–6246, doi:10.1029/1999JA000260.
El-Alaoui, M., M. Ashour-Abdalla, R. J. Walker, V. Peroomian, R. L. Richard, V. Angelopoulos, and A. Runov (2009), Substorm evolution as revealed by THEMIS satellites and a global MHD simulation, *J. Geophys. Res.*, *114*, A08221, doi:10.1029/2009JA014133.
El-Alaoui, M., R. L. Richard, M. Ashour-Abdalla, M. L. Goldstein, and R. J. Walker (2013), Dipolarization and turbulence in the plasma sheet during a substorm: THEMIS observations and global MHD simulations, *J. Geophys. Res. Space Physics*, *118*, 7752–7761, doi:10.1002/2013JA019322.
Fedder, J. A., S. P. Slinker, J. G. Lyon, and R. D. Elphinstone (1995), Global numerical simulation of the growth phase and the expansion onset for a substorm observed by Viking, *J. Geophys. Res.*, *100*, 19,083–19,094, doi:10.1029/95JA01524.
Fridman, M., and J. Lemaire (1980), Relationship between auroral electrons fluxes and field aligned electric potential difference, *J. Geophys. Res.*, *85*, 664–670, doi:10.1029/JA085iA02p00664.
Fujita, S., and T. Tanaka (2013), Possible generation mechanisms of the Pi2 pulsations estimated from a global MHD simulation, *Earth Planets Space*, *65*, 453–461, doi:10.5047/eps.2012.11.005.
Fujita, S., H. Nakata, M. Itonaga, A. Yoshikawa, and T. Mizuta (2002), A numerical simulation of the Pi2 pulsations associated with the substorm current wedge, *J. Geophys. Res.*, *107*(A3), 1034, doi:10.1029/2001JA900137.
Henderson, M. G. (2012), Auroral substorms, poleward boundary activations, auroral streamers, omega bands, and onset precursor activity, in *Auroral Phenomenology and Magnetospheric Processes: Earth and Other Planets, Geophys. Monogr. Ser.*, vol. 197, edited by A. Keiling et al., pp. 39–54, AGU, Washington, D. C., doi:10.1029/2011GM001165
Hsu, T.-S., and R. L. McPherron (2007), A statistical study of the relation of Pi 2 and plasma flows in the tail, *J. Geophys. Res.*, *112*, A05209, doi:10.1029/2006JA011782.
Hsu, T.-S., R. L. McPherron, V. Angelopoulos, Y. Ge, H. Zhang, C. Russell, X. Chu, and J. Kissinger (2012), A statistical analysis of the association between fast plasma flows and Pi2 pulsations, *J. Geophys. Res.*, *117*, A11221, doi:10.1029/2012JA018173.
Keiling, A. (2012), Pi2 pulsations driven by ballooning instability, *J. Geophys. Res.*, *117*, A03228, doi:10.1029/2011JA017223.
Keiling, A., and K. Takahashi (2011), Review of Pi2 models, *Space Sci. Rev.*, *161*, 63–148, doi:10.1007/s11214-011-9818-4.
Keiling, A., et al. (2006), Association of Pi2 pulsations and pulsed reconnection: Ground and Cluster observations in the tail lobe at 16 R_E, *Ann. Geophys.*, *24*, 3433–3449, doi:10.5194/angeo-24-3433-2006.
Keiling, A., et al. (2008), Correlation of substorm injections, auroral modulations, and ground Pi2, *Geophys. Res Lett.*, *35*, L17S22, doi:10.1029/2008GL033969.
Keiling, A., et al. (2009), Substorm current wedge driven by plasma flow vortices: THEMIS observations, *J. Geophys. Res.*, *114*, A00C22, doi:10.1029/2009JA014114.
Kennel, C. F., and H. E. Petschek (1966), Limit on stably trapped particle fluxes, *J. Geophys. Res.*, *71*, 1–28.
Kepko, L., and M. Kivelson (1999), Generation of Pi2 pulsations by bursty bulk flows, *J. Geophys. Res.*, *104*, 25,021–25,034, doi:10.1029/1999JA900361.
Kepko, L., M. G. Kivelson, and K. Yumoto (2001), Flow bursts, braking, and Pi2 pulsations, *J. Geophys. Res.*, *106*, 1903–1916, doi:10.1029/2000JA000158.
Kepko, L., M. G. Kivelson, R. L. McPherron, and H. E. Spence (2004), Relative timing of substorm onset phenomena, *J. Geophys. Res.*, *109*, A04203, doi:10.1029/2003JA010285.
Kim, K.-H., K. Takahashi, S. Ohtani, and S.-K. Sung (2007), Statistical analysis of the relationship between earthward flow bursts in the magnetotail and low-latitude Pi2 pulsations, *J. Geophys. Res.*, *112*, A10211, doi:10.1029/2007JA012521.
Knight, S. (1973), Parallel electric fields, *Planet. Space Sci.*, *21*(5), 741–750, doi:10.1016/0032-0633(73)90093-7.
Kwon, H.-J., et al. (2012), Local time-dependent Pi2 frequencies confirmed by simultaneous observations from THEMIS probes in the inner magnetosphere and at low-latitude ground stations, *J. Geophys. Res.*, *117*, A01206, doi:10.1029/2011JA016815.
Lee, D.-H., and R. L. Lysak (1999), MHD waves in a three-dimensional dipolar magnetic field: A search for Pi2 pulsations, *J. Geophys. Res.*, *104*, 28,691–28,700, doi:10.1029/1999JA900377.
Lyon, J. G., J. A. Fedder, and C. M. Mobarry (2004), The Lyon-Fedder-Mobarry (LFM) global MHD magnetospheric simulation code, *J. Atmos. Sol. Terr. Phys.*, *66*, 1333–1350, doi:10.1016/j.jastp.2004.03.020.
Lyons, L. R., D. S. Evans, and R. Lundin (1979), An observed relation between magnetic field aligned electric fields and downward electron energy fluxes in the vicinity of auroral forms, *J. Geophys. Res.*, *84*, 457–461, doi:10.1029/JA084iA02p00457.
McPherron, R. L. (1972), Substorm related changes in the geomagnetic tail: The growth phase, *Planet. Space Sci.*, *20*, 1521–1539, doi:10.1016/0032-0633(72)90054-2.
Mende, S. B., H. U. Frey, M. Lampton, J.-C. Gerard, B. Hubert, S. Fuselier, J. Spann, R. Gladstone, and J. L. Burch (2001), Global observations of proton and electron auroras in a substorm, *Geophys. Res. Lett.*, *28*, 1139–1142, doi:10.1029/2000GL012340.
Miyashita, Y., S. Machida, T. Mukai, Y. Saito, K. Tsuruda, H. Hayakawa, and P. R. Sutcliffe (2000), A statistical study of variations in the near and middistant magnetotail associated with substorm onsets: GEOTAIL observations, *J. Geophys. Res.*, *105*, 15,913–15,930, doi:10.1029/1999JA000392.
Nagai, T., M. Fujimoto, R. Nakamura, Y. Saito, T. Mukai, T. Yamamoto, A. Nishida, S. Kokubun, G. D. Reeves, and R. P. Lepping (1998), Geotail observations of a fast tailward flow at $X_{GSM} = -15R_E$, *J. Geophys. Res.*, *103*, 23,543–23,550, doi:10.1029/98JA02246.
Nakamizo, A., and T. Iijima (2003), A new perspective on magnetotail disturbances in terms of inherent diamagnetic processes, *J. Geophys. Res.*, *108*(A7), 1286, doi:10.1029/2002JA009400.
Olson, J. V. (1999), Pi2 pulsations and substorm onsets: A review, *J. Geophys. Res.*, *104*, 17,499–17,520, doi:10.1029/1999JA900086.
Owens, J. H., and J. Fedder (1978), The effects of geomagnetic field aligned potential differences on precipitating magnetospheric particles, *Tech. Rep.*, Navel Research Lab., Memo Rep. 3573.
Raeder, J., J. Berchem, and M. Ashour-Abdalla (1998), The geospace environment modeling grand challenge: Results from a global geospace circulation model, *J. Geophys. Res.*, *103*, 14,787–14,798, doi:10.1029/98JA00014.
Ream, J. B., R. J. Walker, M. Ashour-Abdalla, M. El-Alaoui, M. G. Kivelson, and M. L. Goldstein (2013), Generation of Pi2 pulsations by intermittent earthward propagating dipolarization fronts: An MHD case study, *J. Geophys. Res. Space Physics*, *118*, 6364–6377, doi:10.1002/2013JA018734.
Robinson, R. M., R. R. Vondrak, K. Miller, T. Dabbs, and D. Hardy (1987), On calculating ionospheric conductances from the flux and energy of precipitating electrons, *J. Geophys. Res.*, *92*, 2565–2569, doi:10.1029/JA092iA03p02565.
Saito, T., and S. Matsushita (1968), Solar cycle effects on geomagnetic Pi2 pulsations, *J. Geophys. Res.*, *73*, 267–286, doi:10.1029/JA073i001p00267.
Saito, T., K. Yumoto, and Y. Koyama (1976), Magnetic pulsation Pi 2 as a sensitive indicator of magnetospheric substorm, *Planet. Space Sci.*, *24*, 1025–1029, doi:10.1016/0032-0633(76)90120-3.

Sakurai, T., and T. Saito (1976), Magnetic pulsations Pi2 and substorm onset, *Planet. Space Sci.*, *24*, 573–575, doi:10.1016/0032-0633(76)90135-5.

Shiokawa, K., W. Baumjohann, and G. Haerendel (1997), Braking of high-speed flows in the near-Earth tail, *Geophys. Res. Lett.*, *24*, 1179–1182, doi:10.1029/97GL01062.

Slinker, S. P., J. A. Fedder, B. A. Emery, K. B. Baker, D. Lummerzheim, J. G. Lyon, and F. J. Rich (1999), Comparison of global MHD simulations with AMIE simulations for the events of May 19–20, 1996, *J. Geophys. Res.*, *104*, 28,379–28,396, doi:10.1029/1999JA900403.

Solovyev, S. I., D. G. Baishev, E. S. Barkova, N. E. Molochushkin, and K. Yumoto (2000), Pi2 magnetic pulsations as response on spatio-temporal oscillations of auroral arc current system, *J. Geophys. Res.*, *27*, 1839–1842, doi:10.1029/2000GL000037.

Southwood, D. J., and W. F. Stuart (1980), Pulsations at the substorm onset, in *Dynamics of the Magnetosphere*, edited by S.-I. Akasofu, pp. 341–355, Springer, Netherlands.

Sutcliffe, P. R. (1975), The association of harmonics in Pi 2 power spectra with the plasmapause, *Planet. Space Sci.*, *23*, 1581–1587, doi:10.1016/0032-0633(75)90085-9.

Sutcliffe, P. R., and K. Yumoto (1991), On the cavity mode nature of low-latitude Pi2 pulsations, *J. Geophys. Res.*, *96*, 1543–1551, doi:10.1029/90JA02007.

Takahashi, K., S.-I. Ohtani, and K. Yumoto (1992), AMPTE CCE observations of Pi 2 pulsations in the inner magnetosphere, *Geophys. Res. Lett.*, *19*, 1447–1450, doi:10.1029/92GL01283.

Uozumi, T., H. Kawano, A. Yoshikawa, M. Itonaga, and K. Yumoto (2007), Pi 2 source region in the magnetosphere deduced from CPMN data, *Planet. Space Sci.*, *55*, 849–857, doi:10.1016/j.pss.2006.03.016.

Uozumi, T., et al. (2009), Propagation characteristics of Pi 2 pulsations observed at high- and low-latitude MAGDAS/CPMN stations: A statistical study, *J. Geophys. Res.*, *114*, A11207, doi:10.1029/2009JA014163.

Uozumi, T., et al. (2011), AKR modulation and global Pi2 oscillation, *J. Geophys. Res.*, *116*, A06214, doi:10.1029/2010JA016042.

Walker, R. J., M. Ashour-Abdalla, M. El Alaoui, and F. V. Coroniti (2006), Magnetospheric convection during prolonged intervals with southward interplanetary magnetic field, *J. Geophys. Res.*, *111*, A10219, doi:10.1029/2005JA011541.

Wiltberger, M., R. S. Weigel, W. Lotko, and J. A. Fedder (2009), Modeling seasonal variations of auroral particle precipitation in a global-scale magnetosphere-ionosphere simulation, *J. Geophys. Res.*, *114*, A01204, doi:10.1029/2008JA013108.

Yeoman, T. K., and D. Orr (1989), Phase and spectral power of mid-latitude Pi2 pulsations—Evidence for a plasmaspheric cavity resonance, *Planet. Space Sci.*, *37*, 1367–1383, doi:10.1016/0032-0633(89)90107-4.

Yumoto, K., T. Saito, K. Takahashi, F. W. Menk, and B. J. Fraser (1989), Some aspects of the relation between Pi 1–2 magnetic pulsations observed at $L = 1.3$–2.1 on the ground and substorm-associated magnetic field variations in the near-Earth magnetotail observed by AMPTE CCE, *J. Geophys. Res.*, *94*, 3611–3618, doi:10.1029/JA094iA04p03611.